Investigation of partially coherent vector vortex beams with non-isotropic states of spatial correlation

MANISHA,[1,*] ⓘ STUTI JOSHI,[1] ⓘ SABA N KHAN,[1,2] ⓘ
BHASKAR KANSERI,[1] ⓘ AND P SENTHILKUMARAN[1,3] ⓘ

[1]*Department of Physics, Indian Institute of Technology Delhi, Hauz Khas, New Delhi- 110016, India*
[2]*School of Physics and Astronomy, University of St Andrews, North Haugh, St Andrews KY16 9SS, UK*
[3]*Optics and Photonics Center, Indian Institute of Technology Delhi, Hauz Khas, New Delhi- 110016, India*
[*]*manisha12101994@gmail.com*

Abstract: In this work, the far-field properties of non-isotropic partially coherent vector vortex beams (PCVVBs) are investigated both theoretically and experimentally. The term non-isotropic signifies that the spatial correlations between the parallel and orthogonal electric field components are distinguishable. It is found that self-orientation and shaping of intensity profile, correlation-induced polarization and depolarization are highly dependent on both the non-isotropic correlation parameters and Poincaré-Hopf index (PHI) of the beam. The simultaneous depolarization and polarization effects are due to the difference in the input correlation parameters that alter the state of polarization (SOP) and degree of polarization (DOP) distributions. The experimental results are in good agreement with the theoretical predictions. The distinguishability of correlation parameters at the source plane leads to significant changes on its intensity profile, DOP, and SOP distributions on far-field propagation, which may found potential applications in beam shaping, detecting and imaging atmospheric lidar, optical imaging and directional transportation where the self-rotation characteristic of beam plays an important role.

1. Introduction

Optical field manipulation has become one of the eminent topics of research in recent years [1,2]. The manipulation of the correlation properties at the source plane leads to significant changes in the correlation as well as polarization properties at the observation plane [3,4]. These outcomes are the direct manifestations of the well-known unified theory of coherence and polarization proposed by Wolf [5]. This seminal theory then provided ways to study the statistical properties such as intensity distribution, degree of polarization (DOP), and state of polarization (SOP) of partially coherent beams in both the scalar and vector domains [6–10]. The studies on the generation, detection, and propagation of partially coherent (PC) beam in the scalar domain using Gaussian-Schell model (GSM) beams [11,12] and their vector counter parts using electromagnetic Gaussian-Schell model (EGSM) beams [9,10,13,14] have been investigated in detail. The SOP, DOP, intensity and other statistical properties of PC beams are highly dependent on the input spatial correlation parameters ($\delta_{\alpha\beta}$, (α, $\beta = x$ and y)) [10,15]. Unlike the case of isotropic beams ($\delta_{xx} = \delta_{yy}$) where in the SOP and DOP changes are hard to find [11,12,16,17], the non-isotropic beams show prominent changes in their statistical properties under far-field propagation [10,18,19]. The term non-isotropic here signifies that the spatial correlations between the parallel and orthogonal electric field components are distinguishable, i.e., $\delta_{xx} \neq \delta_{yy} \neq \delta_{xy}$. The studies were also extended to the partially coherent phase singular (vortex) beams where an additional degree of freedom is manifested in the form of orbital angular momentum (OAM) content of vortex beam [20–22]. The oppositely charged vortex beam carrying the orthogonal

spin-angular momentum (SAM) states can be superposed to form inhomogeneously polarized vector vortex beams [23].

Vector vortex beams (VVBs) are the special class of polarization singular beams, where the predominant SOPs are linear with intensity null at the center [23]. Beams carrying polarization singularities have gained considerable scientific interest due to their potential applications in edge enhancement [24], particle trapping [25], free-space optical communication [26], robust structure beam generation [27], high-resolution microscopy [28] and material processing [29]. These VVBs are characterized by Poincaré-Hopf index (PHI) $\eta = \frac{1}{2\pi} \oint \nabla\varphi \cdot dl$, φ being azimuth and the line integral gives the gradient of azimuth around the singularity. More recently, polarization singular VVBs with controlled spatial coherence properties are investigated [30–33]. It is proposed that PCVVBs can be useful in trapping of the particles of different sizes and refractive indices [34], beam shaping [35] and high resolution microscopy [36]. In all these studies on PCVVBs, the correlation properties in the source plane are assumed to be isotropic ($\delta_{xx} = \delta_{yy}$). To the best of our knowledge, there are no studies on the investigation of statistical properties of non-isotropic partially coherent vector vortex beams (non-isotropic PCVVBs). However, it has been shown that the electromagnetic Gaussian Schell-model vortex beam (i.e., $\delta_{xx} \neq \delta_{yy} \neq \delta_{xy}$) is useful to detect a phase object [37]. Additionally, compared to the partially coherent vortex beam with isotropic correlation properties, the non-isotropic partially coherent vortex beams have an advantage of self-orientation of intensity profile in addition to the beam shaping, which can be useful for trapping and rotating particles. Most recently, the advantage of using partially coherent vector beams in atmospheric turbulence is reported [38].

With this motivation, in this work, we detail our investigations on the far-field statistical properties of PCVVBs with non-isotropic state of spatial correlation. On reducing the spatial correlation parameters of the input beam, various effects namely, the self-shaping of the intensity profile, appearance of homogeneous SOP region in the core, an overall depolarization with coherence-induced polarization around the core of the beam are observed. These changes are found to be strongly dependent on both the correlation properties at the source plane and the PHI (η) of the non-isotropic PCVVB. Such a source with partial coherence and partial polarization may be useful in long-distance communication by reducing the scintillation index in atmospheric turbulence [39]. The article is organized as follows: section 2 includes the theoretical framework to study the far-field properties of PCVVBs and the simulated results. The experimental scheme to characterize these non-isotropic beams is presented in section 3. The experimental results which verify the theoretical predictions are discussed in section 4. All the findings are concluded in section 5.

2. Theoretical description: non-isotropic partially coherent vector vortex beams

The electric field of a vector vortex beam can be written as a superposition of orbital angular momentum states in the orthogonal spin angular momentum states [23]

$$
\begin{aligned}
\mathbf{E}(r,\theta) &= \frac{r^{|l|}}{2} \exp\left(-\frac{r^2}{(2\sigma)^2}\right) \left[\frac{1}{\sqrt{2}} \exp\left(\pm il\theta\right)(\hat{x} - i\hat{y}) \pm \frac{1}{\sqrt{2}} \exp\left(\mp il\theta\right)(\hat{x} + i\hat{y}) \right]_{(I/II)}, \\
&= \frac{ir^{|l|}}{2} \exp\left(-\frac{r^2}{(2\sigma)^2}\right) \left[\pm\frac{1}{\sqrt{2}} \exp\left(\pm il\theta\right)(\hat{x} - i\hat{y}) - \frac{1}{\sqrt{2}} \exp\left(\mp il\theta\right)(\hat{x} + i\hat{y}) \right]_{(III/IV)},
\end{aligned}
\tag{1}
$$

where $r^2 = x^2 + y^2$, l, θ and σ are the topological charge, azimuthal angle and beam waist, respectively. The PHI of the resulting beam is such that $|\eta| = |l|$. Since the amplitude distribution for the right circularly polarized (RCP) and left circularly polarized (LCP) components are same, the superposition results in the constant ellipticity fields. By introducing a phase difference between the RCP and LCP component vortex beams and by amplitude scaling, VVBs can be represented by a point on a higher order Poincaré sphere [31,40,41]. Interestingly, the VVBs

of a particular η, have polarization distributions identical to the modes of a fiber. For instance, TE_{0m} (TM_{0m}) mode possesses azimuthal (radial) polarization distribution for $m = 1$ and flower patterned SOP distribution for $m>1$ with $2(m-1)$ number of petals in the pattern and $HE_{2m}^{odd/even}$ modes possess anti-radial(odd)/anti-azimuthal(even) SOP distributions for $m = 1$ and spider-web patterned distribution for $m>1$ with $2(m + 1)$ number of sectors in the web [42,43]. In this context, the mode index $'m'$ is equal to the magnitude of PHI of the beam (i.e., $m = |\eta|$). These polarization distributions can also be generated readily using laser resonators [44,45]. However, their natural occurrence is elusive because their co-dimension is four [46]. In polarization speckles [47], occurrence of C-points singularities is common but V-points singularities are forbidden. In our experiments, we generated V-points by using q-plates as they do not occur naturally. Keeping these facts in mind, we have included these four types of VVBs (generic and higher PHI) in our studies (refer to Eq. (1) for mathematical description of these four types). For a fixed PHI ($|\eta|$), these beams possess different SOP distributions but are intensity degenerate [23].

The correlation properties of a statistically stationary, quasi-monochromatic PCVVB, in the space-frequency domain, are characterized by a 2×2 cross-spectral density (CSD) matrix [5],

$$\mathbf{W}_0(\mathbf{r}_1, \mathbf{r}_2) = \begin{bmatrix} W_{0xx}(\mathbf{r}_1, \mathbf{r}_2) & W_{0xy}(\mathbf{r}_1, \mathbf{r}_2) \\ W_{0yx}(\mathbf{r}_1, \mathbf{r}_2) & W_{0yy}(\mathbf{r}_1, \mathbf{r}_2) \end{bmatrix}. \tag{2}$$

Here, $\mathbf{r}_1(r_1, \theta_1)$, and $\mathbf{r}_2(r_2, \theta_2)$ are two transverse points in the source plane as shown in Fig. 1. $W_{0\alpha\beta}(\mathbf{r}_1, \mathbf{r}_2) = \langle E_\alpha^*(\mathbf{r}_1)E_\beta(\mathbf{r}_2)\rangle, (\alpha, \beta = x, y)$, where, E_α and E_β denote the electric field components in orthogonal directions, the asterisk denotes the complex conjugate and angular brackets are the ensemble averages. In this study the non-isotropic PCVVBs are considered to be generated using EGSM source. The CSD-matrix element of an EGSM beam is given by [48],

$$W_{0\alpha\beta}(\mathbf{r}_1, \mathbf{r}_2) = A_\alpha A_\beta |B_{\alpha\beta}| \exp\left[-\frac{\mathbf{r}_1^2}{4\sigma_\alpha^2} - \frac{\mathbf{r}_2^2}{4\sigma_\beta^2} - \frac{(\mathbf{r}_2 - \mathbf{r}_1)^2}{2\delta_{\alpha\beta}^2}\right], \tag{3}$$

Here A_α and A_β are the characteristic amplitudes of field components, σ_α and σ_β are beam waists, $B_{\alpha\beta}$ is correlation coefficient. All these parameters are independent of position and dependent on wavelength λ. The correlation parameter is defined by $\delta_{\alpha\beta}$. For simplicity, we have taken $\sigma_\alpha = \sigma_\beta = \sigma$ and further $B_{\alpha\beta}$ coefficients must satisfy the following conditions [15],

$$|B_{\alpha\beta}| = 1, \quad \text{for} \quad \alpha = \beta, \quad \text{and} \quad |B_{\alpha\beta}| \le 1, \quad \text{for} \quad \alpha \ne \beta. \tag{4}$$

Also, these correlation parameters can not be chosen arbitrarily. The parameters σ, $\delta_{\alpha\beta}$ and $B_{\alpha\beta}$ must follow realizability conditions given as [49,50],

$$\frac{1}{4\sigma^2} + \frac{1}{\delta_{\alpha\beta}^2} \ll \frac{2\pi^2}{\lambda^2}, \quad \text{and} \quad \sqrt{\frac{\delta_{xx}^2 + \delta_{yy}^2}{2}} \le \delta_{xy} \le \sqrt{\frac{\delta_{xx}\delta_{yy}}{|B_{\alpha\beta}|}}. \tag{5}$$

These restrictions play a crucial role in evolving the propagation properties of EGSM beams. Using equations Eq. (1) to Eq. (7) the CSD matrix elements for non-isotropic partially coherent vector vortex beams (type I) in the source plane can be expressed as,

$$\begin{aligned}
W_{0xx}(\mathbf{r}_1, \mathbf{r}_2) &= \cos(l\theta_1)\cos(l\theta_2)\gamma_{\alpha\beta}(\mathbf{r}_1, \mathbf{r}_2), \\
W_{0yy}(\mathbf{r}_1, \mathbf{r}_2) &= \sin(l\theta_1)\sin(l\theta_2)\gamma_{\alpha\beta}(\mathbf{r}_1, \mathbf{r}_2), \\
W_{0xy}(\mathbf{r}_1, \mathbf{r}_2) &= \cos(l\theta_1)\sin(l\theta_2)\gamma_{\alpha\beta}(\mathbf{r}_1, \mathbf{r}_2), \\
W_{0yx}(\mathbf{r}_1, \mathbf{r}_2) &= \sin(l\theta_1)\cos(l\theta_2)\gamma_{\alpha\beta}(\mathbf{r}_1, \mathbf{r}_2),
\end{aligned} \tag{6}$$

where, $\gamma_{\alpha\beta}(\mathbf{r}_1, \mathbf{r}_2) = \frac{(r_1 r_2)^{|l|}}{(2\sigma)^{2|l|}} \exp(-\frac{r_1^2 + r_2^2 - 2r_1 r_2 \cos(\theta_1 - \theta_2)}{2\delta_{\alpha\beta}^2}) \exp(-\frac{r_1^2 + r_2^2}{4\sigma^2})$. The non-isotropic PCVVB is generated by a source located in the z = 0 plane and propagates close to the z-axis into the half space z>0 as shown in Fig. 1. The CSD matrix elements of non-isotropic PCVVBs at the observation plane can be obtained by using generalized Collins formula given by [51],

$$W_{\alpha\beta}(\boldsymbol{\rho}_1, \boldsymbol{\rho}_2, z) = \frac{1}{\lambda^2 B^2} \int_0^\infty \int_0^\infty \int_0^{2\pi} \int_0^{2\pi} W_{0\alpha\beta}(\mathbf{r}_1, \mathbf{r}_2) \exp\left[\frac{ikD}{2B}(\rho_2^2 - \rho_1^2) - \frac{ikA}{2B}(\mathbf{r}_1^2 - \mathbf{r}_2^2)\right]$$

$$\times \exp\left[\frac{ik}{B}(r_1\rho_1 \cos(\phi_1 - \theta_1) - r_2\rho_2 \cos(\phi_2 - \theta_2))\right] r_1 r_2 \mathrm{d}r_1 \mathrm{d}r_2 \mathrm{d}\theta_1 \mathrm{d}\theta_2,$$

$$(7)$$

where, $k = \frac{2\pi}{\lambda}$, λ is wavelength and $\boldsymbol{\rho}_1(\rho_1, \phi_1)$ and $\boldsymbol{\rho}_2(\rho_2, \phi_2)$ are the coordinates of two transverse points in the observation plane (see Fig. 1). The elements of the transfer matrix for far-field propagation are $A = D = 0, B = f$ and $C = -\frac{1}{f}$ [30]. The total intensity, I($\boldsymbol{\rho}$) can be expressed in terms of CSD matrix elements as [8],

$$I(\boldsymbol{\rho}) = W_{xx}(\boldsymbol{\rho}, \boldsymbol{\rho}) + W_{yy}(\boldsymbol{\rho}, \boldsymbol{\rho}). \tag{8}$$

The far-field intensity distributions for various index non-isotropic PCVVBs on changing the correlation parameter δ_{xx} are shown in the Fig. 2(A). Here, we have discussed three cases, when $\delta_{xx} > \delta_{yy}$ (row (A1)), $\delta_{xx} = \delta_{yy}$ (row (A2)), and $\delta_{xx} < \delta_{yy}$ (row (A3)). Note that the case where $\delta_{xx} = \delta_{yy}$ (row(A2)) refers to the isotropic PCVVB, is also shown for comparision. Unlike the case of isotropic PCVVBs, for non-isotropic PCVVBs, one can observe the maximum and minimum intensity regions symmetrically along the azimuthal direction [33]. The line scans are shown in each distribution along the direction of maximum (white) and minimum (brown) change in intensity. The number of these maximum (or minimum) intensity regions (N) are directly related to the PHI of the beam as $|\eta| = \frac{N}{2}$. The angular position of the maximum and minimum (minimum and maximum) intensity regions along the azimuthal direction for $\delta_{xx} > \delta_{yy}$ ($\delta_{xx} < \delta_{yy}$) can be given by $\frac{\pi(n-1)}{|\eta|}$ and $\frac{\pi(2n-1)}{2|\eta|}$ respectively $\forall \, n = 1, 2, 3 \cdots$ so on. Here, we introduce a parameter χ_a pertaining to the nonuniform intensity distribution along the azimuthal direction. The parameter χ_a is the ratio of minimum and maximum intensity values along the azimuthal direction of the doughnut ring of non-isotropic PCVVBs i.e., ($\chi_a = \frac{I^{\min}}{I^{\max}}$). It is observed that, the χ_a parameter decreases with the decrease in the correlation parameters, for instance $\chi_a^{(\text{row (A3)})} < \chi_a^{(\text{row(A1)})}$. Further, it is observed that the the maximum and minimum intensity regions in the intensity distribution get rotated by an angle of $\frac{\pi}{2|\eta|}$ for $\delta_{xx} < \delta_{yy}$ (row $A1$) with respect to the case when $\delta_{xx} > \delta_{yy}$ (row $A3$). This aspect can be used to predict which component of electric fields have higher correlation between them (δ_{xx} or δ_{yy}). When $\delta_{xx} = \delta_{yy} = \delta_{xy}$ (row $A2$), the intensity distribution is azimuthally symmetric. Further, to study the variation of χ_a parameter with PHI (η), the line profiles of intensities for various PHI non-isotropic PCVVBs are plotted in Fig. 2(B). The intensity profiles for each are shown in the insets of Fig. 2(B). The line profiles are taken along the direction of maximum (solid curve) and minimum (dotted curve) change in intensity for $|\eta| = 1$ (blue), $|\eta| = 2$ (red) and $|\eta| = 3$ (green). The peak values along the direction of maximum and minimum intensity change are highlighted with cyan and pink circles respectively. It is observed, that the difference between the maximum and minimum intensity values increases with the increases in the PHI of beam, such that $\chi_a^{|\eta|=1} > \chi_a^{|\eta|=2} > \chi_a^{|\eta|=3}$. So, asymmetry in intensity distribution is seen to be more prominent for higher index non-isotropic PCVVBs. Similar to the case of isotropic PCVVBs [33], the dark core region in intensity distribution of non-isotropic PCVVBs increases with increasing PHI (see Fig. 2).
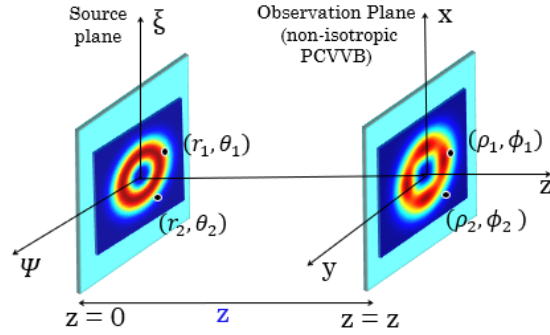
Fig. 1. The coordinate representation of source plane and observation plane considering propagation of non-isotropic PCVVB from z = 0 plane into z>0 space.
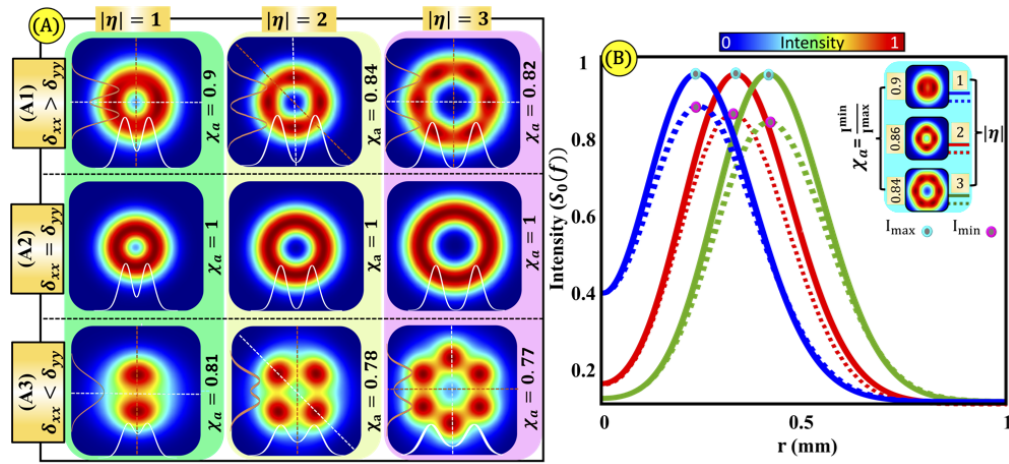

Fig. 2. (A) The far field intensity distributions of various index non-isotropic PCVVBs ($|\eta| = 1, 2, 3$) for correlation widths, rows-(A1) $\delta_{xx} = 3.4$ mm, $\delta_{yy} = 2.7$ mm, $\delta_{xy} = 3.1$ mm (A2) $\delta_{xx} = \delta_{yy} = \delta_{xy} = 3.4$ mm (A3) $\delta_{xx} = 0.8$ mm, $\delta_{yy} = 1.6$ mm, $\delta_{xy} = 1.2$ mm. (B) The line profiles showing the non-uniformity of intensity distribution for non-isotropic PCVVBs of $|\eta| = 1$ (blue curves), $|\eta| = 2$ (red curves), $|\eta| = 3$ (green curves) at correlation parameters $\delta_{xx} = 3$ mm, $\delta_{yy} = 2.1$ mm, $\delta_{xy} = 2.5$ mm. Solid curves (line scan along maximum change in intensity) and dotted curves (line scan along minimum change in intensity).

The degree of polarization can be calculated using CSD matrix as [5],

$$P(\boldsymbol{\rho}) = \sqrt{1 - \frac{4\text{Det}[\mathbf{W}(\boldsymbol{\rho}, \boldsymbol{\rho})]}{(\text{Tr}[\mathbf{W}(\boldsymbol{\rho}, \boldsymbol{\rho})])^2}}, \tag{9}$$

where Det and Tr represent the determinant and trace of the CSD matrix, respectively. The influence of correlation parameters and PHI on the far-field DOP distribution of non-isotropic PCVVBs is shown in the Fig. 3(A). Here again three cases with $\delta_{xx} > \delta_{yy}$ ($A_{11} - B_{11}$), $\delta_{xx} = \delta_{yy}$ ($A_{21} - B_{21}$) and $\delta_{xx} < \delta_{yy}$ ($A_{31} - B_{31}$) for $|\eta| = 1, 2, 3$ are discussed. The line profiles along the direction of maximum DOP-change are shown with white dotted curves over every distribution. The DOP profile is such that DOP possesses a low value at the center which increases towards the radial direction, reaches the maximum value, and then falls off towards the edge of the beam. Unlike isotropic-PCVVBs [33], the non-isotropic PCVVBs have azimuthally asymmetric DOP

distributions. The physical reason for such a change is that the three independent components of the CSD matrix "spread" with different rates along the propagation direction [10]. In addition to the overall depolarization, correlation-induced polarization [52] is observed around the core of the beam for very low values of correlation parameters as can be seen in row (3) ($A_{31} - A_{33}$) of Fig. 3(A). The correlation-induced polarization refers to the fact that the central region of the beam starts acquiring polarization gradually where initially the beam had zero-DOP. Similar to the intensity distributions of non-isotropic PCVVBs, the number of maximum DOP regions in the doughnut ring increases as two times the PHI of the input beam. The strength of polarization effects at the core becomes more prominent for a higher index non-isotropic PCVVBs, (see Fig. 3 (A_{33})). Unlike intensity profiles which have high intensity lobes oriented along the direction dictated by higher correlation parameter, the DOP distribution does not readily carry this information of correlation parameters. The DOP distribution is governed by the contributions from both parallel and orthogonal spatial correlation parameters. For comparison, the far-field DOP distribution of linearly polarized (LP) EGSM is also plotted in Fig. 3(B). The DOP distribution of a LP-EGSM possesses maximum value at the center and drops radially. The maximum value of DOP remains unaffected by varying the source correlation parameters. However, a significant DOP variation in the transverse direction is reported for a partially polarized EGSM beam in a 2f-geometry [53]. The coherence-induced polarization and depolarization effect for non-isotropic PCVVBs can be appreciated by comparing Fig. 3(A) and 3(B).
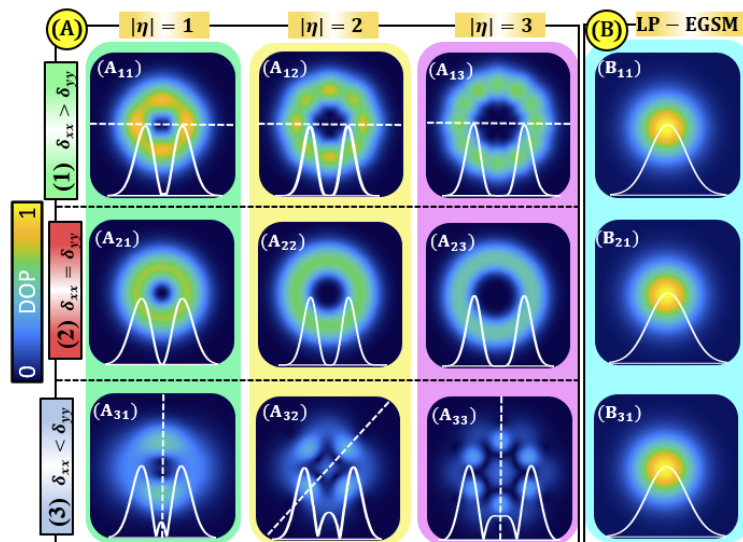

Fig. 3. The degree of polarization distribution of (A) various index non-isotropic PCVVBs ($|\eta| = 1, 2, 3$), (B) linearly polarized EGSM beam. The correlation parameters for the density plots in respective rows are: (1) $\delta_{xx} = 3.4$ mm, $\delta_{yy} = 2.7$ mm, $\delta_{xy} = 3.1$ mm, (2) $\delta_{xx} = \delta_{yy} = 2.5$ mm and (3) $\delta_{xx} = 0.8$ mm, $\delta_{yy} = 1.6$ mm, $\delta_{xy} = 1.2$ mm.

The Stokes parameters, which are related to the polarized component of the intensity, can be obtained from the CSD matrix elements as [8],

$$
\begin{aligned}
S_0(\boldsymbol{\rho}) &= W_{xx}(\boldsymbol{\rho},\boldsymbol{\rho}) + W_{yy}(\boldsymbol{\rho},\boldsymbol{\rho}), \\
S_1(\boldsymbol{\rho}) &= W_{xx}(\boldsymbol{\rho},\boldsymbol{\rho}) - W_{yy}(\boldsymbol{\rho},\boldsymbol{\rho}), \\
S_2(\boldsymbol{\rho}) &= W_{xy}(\boldsymbol{\rho},\boldsymbol{\rho}) + W_{yx}(\boldsymbol{\rho},\boldsymbol{\rho}), \\
S_3(\boldsymbol{\rho}) &= i(W_{yx}(\boldsymbol{\rho},\boldsymbol{\rho}) - W_{xy}(\boldsymbol{\rho},\boldsymbol{\rho})).
\end{aligned}
\tag{10}
$$

The Stokes phase ϕ_{12} which gives the distribution of azimuth around singularity can be obtained from the Stokes parameters as,

$$
\phi_{12} = \arctan\left(\frac{S_2}{S_1}\right).
\tag{11}
$$

3. Experimental generation of non-isotropic PCVVBs

Experimental setup for generating the non-isotropic PCVVBs is shown in the Fig. 4. A linearly polarized laser beam from He-Ne laser ($\lambda = 632.8$ nm) is collimated using a spatial filtering assembly (SF), pin hole and a lens (L1) (part A). The collimated beam is then, directed towards a 50 : 50 polarizing beam splitter (PBS) of a Mach-Zehnder type interferometer (MZI), that divides the beam into two orthogonally polarized beams. The two beams are combined at the output of MZI by a beam splitter (BS) and then directed towards a rotating ground glass diffuser (RGGD). RGGD introduces spatially incoherent features to the beam that developes partial coherence at the source plane (SP) using van Cittert-Zernike theorem [54]. The lenses L2 ($f_2 = 100$ mm) and L3 placed ($f_3 = 100$ mm) in the horizontal and vertical arms of the MZI are used to focus the x and y-polarized beams at RGGD respectively. In our experiment, we fix the position of lens L3 with its focus at RGGD and varied the position of lens L2 to change the spot-size of the x-polarized beam. Thus, the spot-sizes of x and y-polarized beams on RGGD are different and one can control the correlation parameters δ_{xx}, δ_{yy} and δ_{xy} at the source plane. The light scattered from RGGD is collimated by a lens L4 ($f_4 = 200$ mm), such that the resultant beam falling on SP will become non-isotropic ($\delta_{xx} \neq \delta_{yy} \neq \delta_{xy}$). A non-isotropic vector vortex beam is generated by placing spatially varying waveplate (SWP) at the source plane (part B). SWP is constructed using segmented half wave plates (HWPs), with their fast axis oriented in a particular direction [55]. The generated beam is focused by a lens L5 ($f_5 = 200$ mm) to obtain the far-field Stokes parameters. The Stokes parameters ($S_j, j = 0, 1, 2, 3$) for non-isotropic PCVVB are recorded using Stokes camera (SC) (SALSA Stokes camera 1040×1040, Bossa Nova Technologies, USA). SC is a combination of quarter wave plate and polarizer, whose prescribed orientations calculates all the four Stokes parameters, ellipticities, and azimuth.

In order to measure the correlation between the parallel and orthogonal electric field components at the source plane, the beam is passed through a thin lens L6 with focal length f_6 and is further splits into two orthogonally polarized beams by PBS2 (part C). The transmitted and reflected beams from PBS2 arrive at two charge-coupled devices CCD1 (Thorlabs, BC106N-VIS/M, M00491589) and CCD2 (Thorlabs, BC106N-VIS/M, M00613634) respectively. The distances from the source plane to lens L6 and from L6 to CCD's are $2f_6$ (i.e., 4f-imaging system). The output signals from CCD1 and CCD2 are then sent to the personal computer to measure the second-order correlation functions [56]. In our experiment, CCD1 and CCD2 capture simultaneously the x-component and y-component of the intensity of the generated EGSM beams, respectively. We have recorded 1000 instantaneous and continuous images for various spot-sizes (by translating lens L2) at the RGGD and also corresponding to the parallel and orthogonal intensities. The recorded images are then processed in MATLAB to evaluate the correlation functions μ_{xx}, μ_{yy} and μ_{xy}, which give the corresponding correlation parameters $\delta_{xx}, \delta_{yy}, \delta_{xy}$
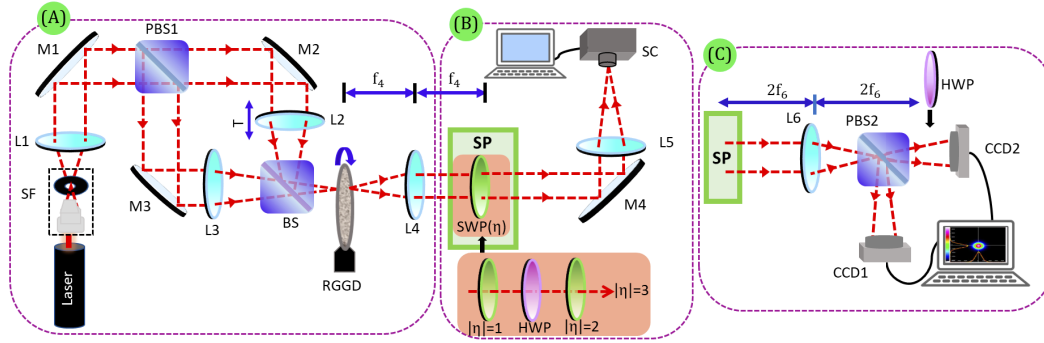
Fig. 4. Schematic of the experimental setup to (A) generate partially coherent electromagnetic beam with non-isotropic characteristics (B) generate non-isotropic PCVVB (C) measure degree of coherence. Abbreviations are- SF: spatial filtering, L1, L2, L3, L4, L5: lenses, M1, M2, M3, M4: mirrors, PBS: polarizing beam splitter, BS: beam splitter, T: translation, RGGD: rotating ground glass diffuser, SP: source plane, HWP: half-wave plate, SWP: spatially varying-HWP, SC: Stokes camera. The non-isotropic PCVVB of $|\eta| = 3$ is generated using two SWPs of $|\eta| = 1$ and $|\eta| = 2$ in concatenation with HWP as shown in inset (orange background) of part (B). The correlation parameters δ_{xx} and δ_{yy} are measured by inserting a HWP in y and x-polarized arms respectively in part (C).
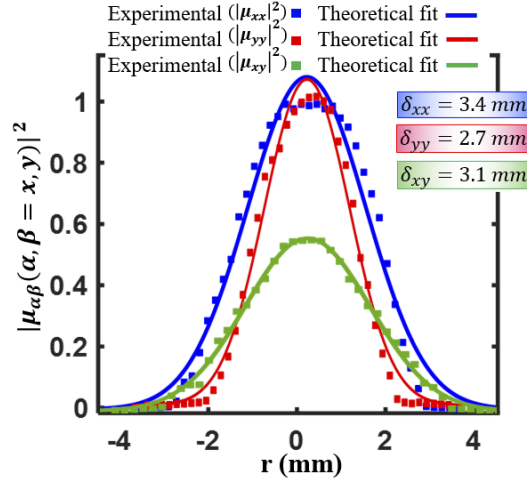

Fig. 5. Measurement of square of correlation functions $|\mu_{xx}|^2$ (red), $|\mu_{yy}|^2$ (blue) and $|\mu_{xy}|^2$ (green). The filled squares are the experimental data points and the solid curves are the theoretical fit.

respectively. The square of degree of correlation can be calculated as [56],

$$|\mu_{\alpha\beta}(r_1, r_2 = 0)|^2 = \frac{1}{N} \frac{\sum_{n=1}^{N} I_{\alpha}^{(n)}(x_1, y_1) I_{\beta}^{(n)}(0, 0)}{\bar{I}_{\alpha}(x_1, y_1) \bar{I}_{\beta}(0, 0)} - 1, (\alpha, \beta = x, y); \qquad (12)$$

where $\bar{I}_{\alpha}(x_1, y_1) = \dfrac{\sum_{n=1}^{N} I_{\alpha}^{(n)}(x_1, y_1)}{N}$ is the average of all realizations at a specific spatial point and

$\bar{I}_{\beta}(0, 0) = \dfrac{\sum_{n=1}^{N} I_{\beta}^{(n)}(0, 0)}{N}$ is the average of all realizations at central point. The curves depicting

square of degree of correlation ($|\mu_{xx}|^2$ (red), $|\mu_{yy}|^2$ (blue) and $|\mu_{xy}|^2$ (green)) at the source plane are shown in Fig. 5. One can find that the distribution of the square of degree of coherence follows the Gaussian profile. The correlation parameters are the measure of full width at half maxima (FWHM) of these Gaussian distributions, obtained by fitting the curves with Eq. (3) for the experimental parameters used. The experimentally obtained correlation parameters are: $\delta_{xx} = 3.4$ mm, $\delta_{yy} = 2.7$ mm, $\delta_{xy} = 3.1$ mm. The calculated parameters satisfy the realizability conditions given in Eqs.(4)–(5). In our experiment, we have obtained various sets of correlation parameters by changing the spot-size of the horizontally polarized beam falling on the RGGD by translating lens L2 (refer to Fig. 4).

4. Results and discussion

The experimental and theoretical results of the normalized intensity distribution for non-isotropic PCVVBs (type I and type III (positive index) along with the component intensities I_x and I_y) are shown in the Fig. 6(A). As mentioned earlier, all the four types of non-isotropic PCVVBs are intensity degenerate, hence the other two types: type II and type IV (negative index) will have the similar distribution as that of the type I and type III, respectively. The intensity distributions corresponding to two cases (a) $\delta_{xx} > \delta_{yy}$ and (b) $\delta_{xx} < \delta_{yy}$ are plotted here. It is observed that the number and position of the maximum intensity points on the ring depends upon the PHI and correlation parameters respectively. For instance, corresponding to the generic non-isotropic PCVVBs ($|\eta| = 1$), the maximum intensity points are oriented along horizontal and vertical directions for $\delta_{xx} > \delta_{yy}$ and $\delta_{xx} < \delta_{yy}$, respectively. These maximum and minimum-intensity values become more prominent with the decrease in the correlation parameters as discussed in section 2. It is interesting to note that the number of maximum intensity regions in the azimuthal direction are exactly two times the PHI of non-isotropic PCVVB. This aspect can be used for the direct measurement of the magnitude of the index of non-isotropic PCVVBs. Notably, the maximum intensity points appearing in the intensity profiles are dominated by the intensity component which has higher correlation between the electric field components, i.e., (I_x for $\delta_{xx} > \delta_{yy}$ and I_y for $\delta_{yy} > \delta_{xx}$). However, the effect of source correlations on the intensity and SOP distributions of the LP-EGSM is not prominent as can be seen in Fig. 6(B).

The experimental and simulated results for polarization distribution and Stokes phase of non-isotropic PCVVBs having positive and negative polarity are shown in the Fig. 7. With the change in the correlation parameters $\delta_{\alpha\beta}$ (from $\delta_{xx} = 3.4$ mm, $\delta_{xx} = 2.7$ mm, $\delta_{xx} = 3.1$ mm to $\delta_{xx} = 1.7$ mm, $\delta_{xx} = 1.1$ mm, $\delta_{xx} = 1.5$ mm), these distributions show significant changes. For higher values of correlation parameters, both SOP and Stokes phase profiles maintain their distributions while for low values of correlation parameters, the Stokes phase undergoes a splitting at the core losing the polarization vortex structure. It is seen that the polarization singular region starts acquiring a homogeneous SOP at the core. The size of the homogeneous distribution region increases with the decreasing correlation parameters. Also, the area of homogeneous SOP distribution region increases for a higher index non-isotropic PCVVB (see the zoom-in encircled region in the inset of Fig. 7). The occurrence of homogeneous SOP at the core indicates a correlation-induced polarization effect around the center of the beam.

To detail this aspect next in the Fig. 8, the line-profiles along the direction of maximum variation in DOP are plotted for the generic and higher-index ($|\eta| = 1, 2, 3$) non-isotropic PCVVBs. One can observe that the correlation-induced depolarization effect [31] is more prominent in a higher PHI non-isotropic PCVVBs. The maximum DOP-value is dependent on the correlation parameters ($\delta_{\alpha\beta}$) of the input beam. The area of central dark core region of DOP increases with increasing PHI. But unlike the isotropic PCVVBs [33], in case of non-isotropic PCVVBs, the DOP at the center starts gradually increasing for lower values of correlation parameters (see green curve in Fig. 8(A–C)). Such transformation is due to the difference between the correlations of parallel and orthogonal electric field components [37,57], which results in
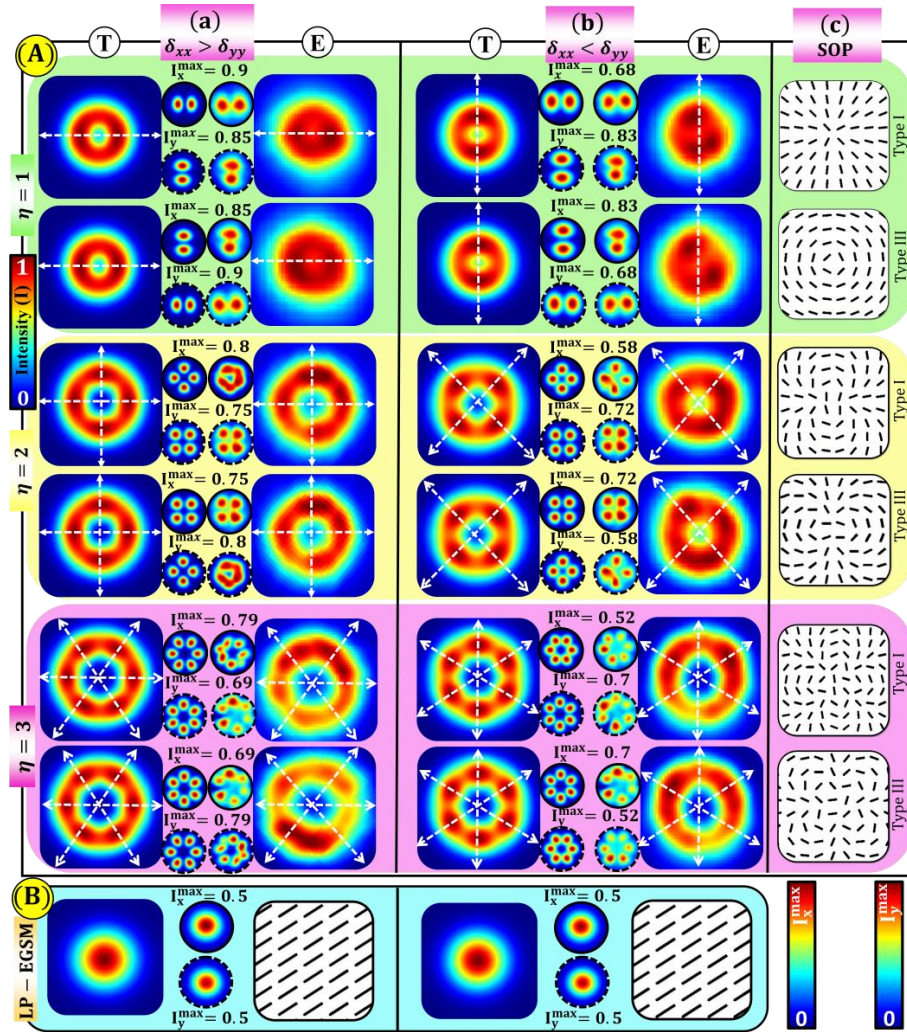
Fig. 6. (A) Theoretical (T) and experimental (E) results for normalized intensity distribution along with its components I_x (solid black border) and I_y (dashed black border) for positive index (type I and type III) non-isotropic PCVVBs of $\eta = 1, 2, 3$ for $\delta_{xx} > \delta_{yy}$ in column (a) and for $\delta_{xx} < \delta_{yy}$ in column (b). The simulated SOP distributions for considered beams are shown in column (c). The intensity components of type I are orthogonal to that of type III. The white dashed lines indicates the directions of maximum intensity change. (B) Intensity and SOP distribution for linearly polarized EGSM beam are also plotted to distinguish the unique feature that non-isotropic beam possesses due to their non-isotropic and vector vortex nature. The coherence induced depolarization effects are neglibible for the EGSM beams.
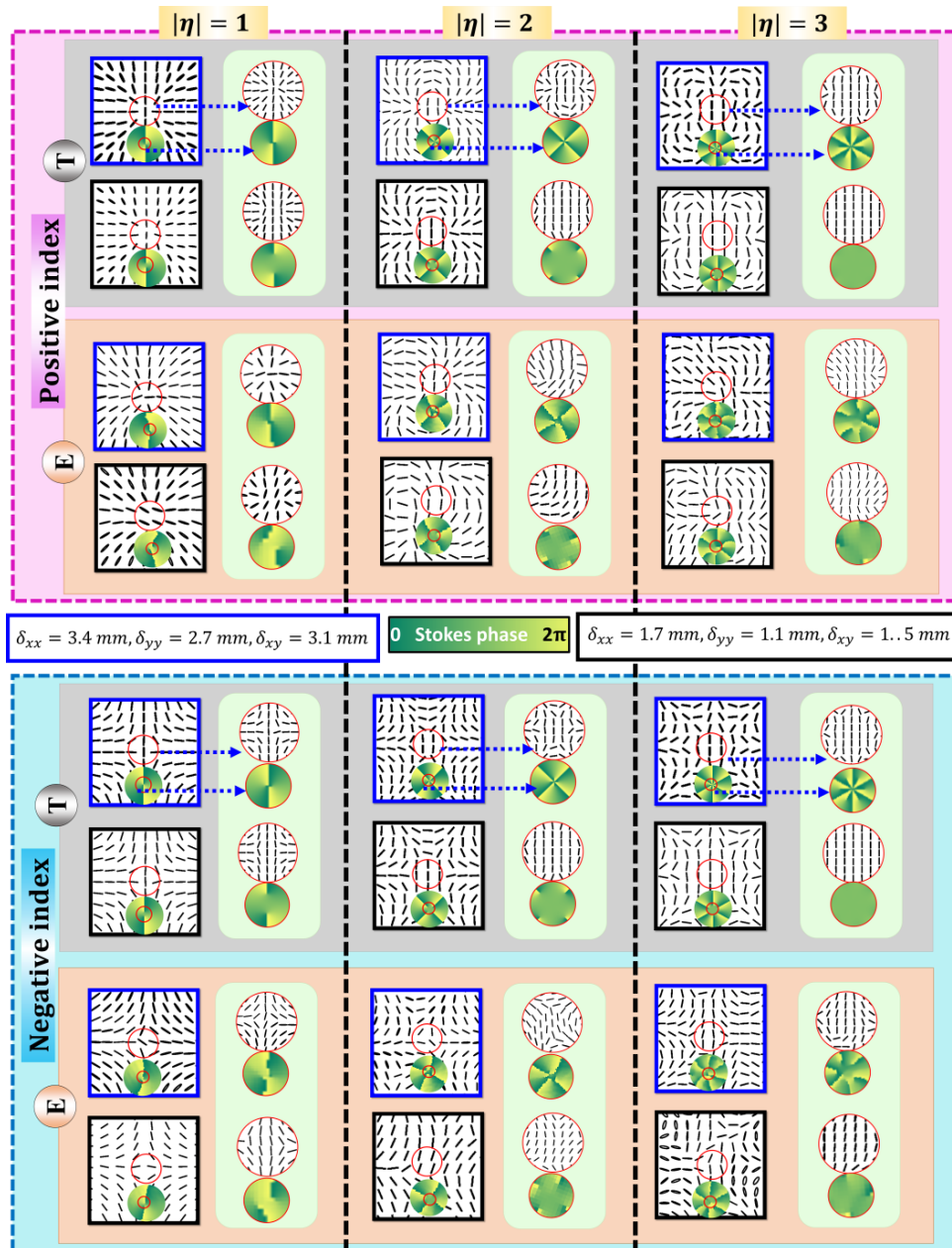
Fig. 7. The theoretical (T) and experimental (E) results for the SOP distributions and corresponding Stokes phases (insets) of various index non-isotropic PCVVBs ($|\eta| = 1, 2, 3$) for correlation parameters $\delta_{xx} = 3.4\,\text{mm}, \delta_{yy} = 2.7\,\text{mm}, \delta_{xy} = 3.1\,\text{mm}$ and $\delta_{xx} = 1.7\,\text{mm}, \delta_{yy} = 1.1\,\text{mm}, \delta_{xy} = 1.5\,\text{mm}$. The zoomed distribution of SOP and Stokes phase at the central region are shown in the right column (green background) of each theoretical and experimental results. The magenta and blue backgrounds differentiate the positive and negative index PCVVBs, respectively.

the different spread rates for CSD matrix elements with propagation and hence modifies the polarization properties [10]. The coherence-induced polarization effect becomes more prominent for the higher index non-isotropic PCVVBs (refer Fig. 8(C)-green curve). The appearance of homogeneous polarization region in Fig. 7, results in flattened DOP-profile around the center which can be clearly seen in Fig. 8. Thus, the far-field statistical properties (intensity profiles, DOP and SOP distributions) of non-isotropic PCVVBs can be controlled through the correlation parameters and PHI of the input beam.
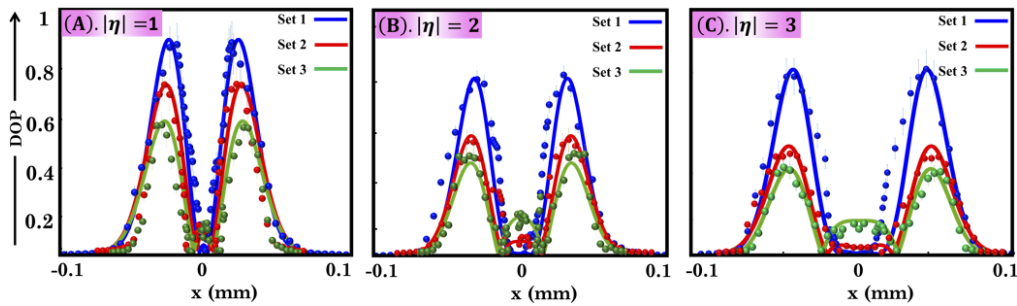

Fig. 8. The DOP profiles for non-isotropic PCVVBs having (A) $|\eta| = 1$, (B) $|\eta| = 2$, and (C) $|\eta| = 3$ for set 1 ($\delta_{xx} = 3.4$ mm, $\delta_{yy} = 2.7$ mm, $\delta_{xy} = 3.1$ mm), set 2 ($\delta_{xx} = 1.8$ mm, $\delta_{yy} = 1.3$ mm, $\delta_{xy} = 1.5$ mm) and set 3 ($\delta_{xx} = 1.5$ mm, $\delta_{yy} = 0.8$ mm, $\delta_{xy} = 1.2$ mm). Profiles are taken along the direction of maximum DOP change. Solid lines are theoretical predictions and filled circles are the experimental data points.

5. Conclusion

The far-field statistical properties namely, intensity profile, SOP and DOP distributions of non-isotropic PCVVBs have been investigated. It is found that the beam's intensity profile, DOP, and SOP distributions are dependent on both the correlation parameters and PHI of the input beam. The non-isotropic nature of PCVVBs is an important factor to consider since it results in azimuthally asymmetric, coherence-induced degradation of intensity and DOP profiles. This aspect can be used to determine the magnitude of PHI of the input beam. The non-isotropic character also introduces a self-orientation of the beam which will be useful for the measurement of directional properties and rotation of particles. Further, the non-isotropic PCVVBs undergo SOP change near the core of the beam but the overall structure is maintained at the periphery of the beam. The experimental results are found to be in good agreement with the theoretical predictions. The study may be useful in the areas that are associated with the correlation and polarization properties of the beam such as FSO communication, atmospheric lidar detection and imaging.

Disclosures. The authors declare no conflicts of interest.

Data availability. Data underlying the results presented in this paper are not publicly available at this time but may be obtained from the authors upon reasonable request.

References

1. W. Gao, A. Imamoglu, H. Bernien, and R. Hanson, "Coherent manipulation, measurement and entanglement of individual solid-state spins using optical fields," Nat. Photonics **9**(6), 363–373 (2015).
2. J. Liu, Z. Li, H. Fan, and G. Zhang, "Coherent optical field manipulation and optical information processing based on electromagnetically-induced transparency effect in Pr^{3+}:Y_2SiO_5 crystal," Appl. Sci. **8**(7), 1179 (2018).

3. Y. Liu, Y. Chen, F. Wang, Y. Cai, C. Liang, and O. Korotkova, "Robust far-field imaging by spatial coherence engineering," Opto-Electron. Adv. **4**(12), 210027 (2021).

4. A. Forbes, M. de Oliveira, and M. R. Dennis, "Structured light," Nat. Photonics **15**(4), 253–262 (2021).

5. E. Wolf, "Unified theory of coherence and polarization of random electromagnetic beams," Phys. Lett. A **312**(5-6), 263–267 (2003).

6. B. Kanseri and H. C. Kandpal, "Experimental determination of electric cross-spectral density matrix and generalized stokes parameters for a laser beam," Opt. Lett. **33**(20), 2410–2412 (2008).

7. S. Joshi, B. Yadav, M. Verma, M. S. Khan, and H. C. Kandpal, "Effect of polarization on spectral anomalies of diffracted stochastic electromagnetic beams," J. Opt. **15**(3), 035405 (2013).

8. E. Wolf, *Introduction to the Theory of Coherence and Polarization of Light* (Cambridge University Press, 2007).

9. B. Kanseri, *Optical Coherence and Polarization: An Experimental Outlook: Experimental Study of Coherence and Polarization Properties of Optical Fields* (LAP LAMBERT Academic Publishing, 2013).

10. O. Korotkova and E. Wolf, "Changes in the state of polarization of a random electromagnetic beam on propagation," Opt. Commun. **246**(1-3), 35–43 (2005).

11. A. T. Friberg and R. J. Sudol, "Propagation parameters of Gaussian Schell-model beams," Opt. Commun. **41**(6), 383–387 (1982).

12. M. Verma, P. Senthilkumaran, J. Joseph, and H. Kandpal, "Experimental study on modulation of stokes parameters on propagation of a Gaussian Schell-model beam in free space," Opt. Express **21**(13), 15432–15437 (2013).

13. S. K. R. Sethuraj and B. Kanseri, "Characterization of the electromagnetic Gaussian Schell-model beam using first-order interference," J. Opt. Soc. Am. A **37**(3), 458–465 (2020).

14. S. K. R. Sethuraj, R. Joshi, and B. Kanseri, "Direct observation of diffraction-induced far-field polarization effects in electromagnetic beams," Opt. Commun. **495**, 127077 (2021).

15. O. Korotkova, M. Salem, and E. Wolf, "The far-zone behavior of the degree of polarization of electromagnetic beams propagating through atmospheric turbulence," Opt. Commun. **233**(4-6), 225–230 (2004).

16. Y. Cai, Y. Chen, J. Yu, X. Liu, and L. Liu, "Generation of partially coherent beams," Prog. Opt. **62**, 157–223 (2017).

17. O. Korotkova, S. Sahin, and E. Shchepakina, "Multi-Gaussian Schell-model beams," J. Opt. Soc. Am. A **29**(10), 2159–2164 (2012).

18. E. Wolf, "Correlation-induced changes in the degree of polarization, the degree of coherence, and the spectrum of random electromagnetic beams on propagation," Opt. Lett. **28**(13), 1078–1080 (2003).

19. D. F. James, "Change of polarization of light beams on propagation in free space," J. Opt. Soc. Am. A **11**(5), 1641–1643 (1994).

20. X. Liu, J. Zeng, and Y. Cai, "Review on vortex beams with low spatial coherence," Adv. Phys.: X **4**(1), 1626766 (2019).

21. Y. Zhang, O. Korotkova, Y. Cai, and G. Gbur, "Correlation-induced orbital angular momentum changes," Phys. Rev. A **102**(6), 063513 (2020).

22. M. Dong, C. Zhao, Y. Cai, and Y. Yang, "Partially coherent vortex beams: Fundamentals and applications," Sci. China Phys. Mech. Astron. **64**(2), 224201 (2021).

23. P. Senthilkumaran, *Singularities in Physics and Engineering*, 2053-2563 (IOP Publishing, 2018).

24. B. B. Ram and P. Senthilkumaran, "Edge enhancement by negative poincare–hopf index filters," Opt. Lett. **43**(8), 1830–1833 (2018).

25. Q. Zhan, "Trapping metallic rayleigh particles with radial polarization," Opt. Express **12**(15), 3377–3382 (2004).

26. K. Khare, P. Lochab, and P. Senthilkumaran, *Orbital Angular Momentum States of Light*, 2053-2563 (IOP Publishing, 2020).

27. P. Lochab, P. Senthilkumaran, and K. Khare, "Robust laser beam engineering using polarization and angular momentum diversity," Opt. Express **25**(15), 17524–17529 (2017).

28. M. Rutkauskas, C. Farrell, C. Dorrer, K. Marshall, T. R. Lundquist, P. Vedagarbha, and D. T. Reid, "High-resolution subsurface microscopy of cmos integrated circuits using radially polarized light," Opt. Lett. **40**(23), 5502–5505 (2015).

29. R. Drevinskas, J. Zhang, M. Beresna, M. Gecevičius, A. G. Kazanskii, Y. P. Svirko, and P. G. Kazansky, "Laser material processing with tightly focused cylindrical vector beams," Appl. Phys. Lett. **108**(22), 221107 (2016).

30. F. Wang, Y. Cai, Y. Dong, and O. Korotkova, "Experimental generation of a radially polarized beam with controllable spatial coherence," Appl. Phys. Lett. **100**(5), 051108 (2012).

31. S. Joshi, S. N. Khan, Manisha, P. Senthilkumaran, and B. Kanseri, "Coherence-induced polarization effects in vector vortex beams," Opt. Lett. **45**(17), 4815–4818 (2020).

32. S. N. Khan, S. Joshi, B. Kanseri, and P. Senthilkumaran, "Detection of partially coherent polarization singular vector beams using stokes polarimetry," Appl. Phys. Lett. **118**(5), 051104 (2021).

33. S. Joshi, S. N. Khan, P. Senthilkumaran, and B. Kanseri, "Statistical properties of partially coherent polarization singular vector beams," Phys. Rev. A **103**(5), 053502 (2021).

34. M. Dong, D. Jiang, N. Luo, and Y. Yang, "Trapping two types of rayleigh particles using a focused partially coherent anomalous vortex beam," Appl. Phys. B **125**(4), 55–58 (2019).

35. Y. Chen, F. Wang, and Y. Cai, "Partially coherent light beam shaping via complex spatial coherence structure engineering," Adv. Phys.: X **7**(1), 2009742 (2022).

36. S. Segawa, Y. Kozawa, and S. Sato, "Resolution enhancement of confocal microscopy by subtraction method with vector beams," Opt. Lett. **39**(11), 3118–3121 (2014).

37. X. Liu, F. Wang, L. Liu, C. Zhao, and Y. Cai, "Generation and propagation of an electromagnetic Gaussian Schell-model vortex beam," J. Opt. Soc. Am. A **32**(11), 2058–2065 (2015).

38. L. Zhao, Y. Xu, and S. Yang, "Statistical properties of partially coherent vector beams propagating through anisotropic atmospheric turbulence," Optik **227**, 166115 (2021).

39. O. Korotkova, "Scintillation index of a stochastic electromagnetic beam propagating in random media," Opt. Commun. **281**(9), 2342–2348 (2008).

40. G. Milione, H. Sztul, D. Nolan, and R. Alfano, "Higher-order poincaré sphere, stokes parameters, and the angular momentum of light," Phys. Rev. Lett. **107**(5), 053601 (2011).

41. G. Arora, S. Deepa, S. N. Khan, and P. Senthilkumaran, "Detection of degenerate stokes index states," Sci. Rep. **10**(1), 20759 (2020).

42. A. Witkowska, S. Leon-Saval, A. Pham, and T. Birks, "All-fiber LP$_{11}$ mode convertors," Opt. Lett. **33**(4), 306–308 (2008).

43. K. Okamoto, *Fundamentals of Optical Waveguides* (Elsevier, 2021).

44. R. Oron, S. Blit, N. Davidson, A. A. Friesem, Z. Bomzon, and E. Hasman, "The formation of laser beams with pure azimuthal or radial polarization," Appl. Phys. Lett. **77**(21), 3322–3324 (2000).

45. S. Ngcobo, I. Litvin, L. Burger, and A. Forbes, "A digital laser for on-demand laser modes," Nat. Commun. **4**(1), 2289 (2013).

46. M. R. Dennis, "Topological singularities in wave fields," Ph.D. thesis, University of Bristol (2001).

47. F. Flossmann, O. Kevin, M. R. Dennis, and M. J. Padgett, "Polarization singularities in 2d and 3d speckle fields," Phys. Rev. Lett. **100**(20), 203902 (2008).

48. M. Salem, O. Korotkova, A. Dogariu, and E. Wolf, "Polarization changes in partially coherent electromagnetic beams propagating through turbulent atmosphere," Waves in Random Media **14**(4), 513–523 (2004).

49. H. Roychowdhury and O. Korotkova, "Realizability conditions for electromagnetic Gaussian Schell-model sources," Opt. Commun. **249**(4-6), 379–385 (2005).

50. T. Shirai, O. Korotkova, and E. Wolf, "A method of generating electromagnetic Gaussian Schell-model beams," J. Opt. A: Pure Appl. Opt. **7**(5), 232–237 (2005).

51. Q. Lin and Y. Cai, "Tensor ABCD law for partially coherent twisted anisotropic Gaussian schell-model beams," Opt. Lett. **27**(4), 216–218 (2002).

52. S. K. R. Sethuraj, R. Joshi, and B. Kanseri, "Determination of polarization structures of an electromagnetic beam after passing through lens systems," Results Phys. **19**, 103459 (2020).

53. X. Zhao, T. D. Visser, and G. P. Agrawal, "Controlling the degree of polarization of partially coherent electromagnetic beams with lenses," Opt. Lett. **43**(10), 2344–2347 (2018).

54. M. Born and E. Wolf, *Principles of Optics: Electromagnetic Theory of Propagation, Interference and Diffraction of Light* (Elsevier, 2013).

55. F. Cardano, E. Karimi, S. Slussarenko, L. Marrucci, C. de Lisio, and E. Santamato, "Polarization pattern of vector vortex beams generated by q-plates with different topological charges," Appl. Opt. **51**(10), C1–C6 (2012).

56. Y. Chen, F. Wang, L. Liu, C. Zhao, Y. Cai, and O. Korotkova, "Generation and propagation of a partially coherent vector beam with special correlation functions," Phys. Rev. A **89**(1), 013801 (2014).

57. Z. Mei, Y. Mao, and Y. Wang, "Electromagnetic multi-Gaussian Schell-model vortex light sources and their radiation field properties," Opt. Express **26**(17), 21992–22000 (2018).